

GSA Data Repository 2016245

## Formation of a future supercontinent through plate motion–driven flow coupled with mantle downwelling flow

Masaki Yoshida

### METHODS

#### Previous 3-D Mantle Convection Model Reproduced Plate-scale Mantle Flow

In previous 3-D mantle convection simulations, there have been two approaches used for reproducing the actual plate motion and plate-scale mantle flow at the Earth's surface (Glišović and Forte, 2015).

One is to reproduce instantaneous plate motion by buoyancy forces in the mantle alone, which is defined by prescribing actual subducting slab geometries. In that approach, a highly viscous lithosphere needs to be divided by either *a priori* low-viscosity plate boundaries (Yoshida et al., 2001; Yoshida and Nakakuki, 2009) or self-generated low-viscosity boundaries owing to the stress-dependent (i.e., yielding) viscosity (e.g., Rolf and Tackley, 2011) in the finite-volume-based model or mechanically discontinuous faults in the finite-element-based model (e.g., Stadler et al., 2010; Zhong and Davies, 1999). Another approach is to impose the present-day or past plate motion data as a velocity boundary condition at the top surface boundary. In that approach, the imposed plate motion makes a moderately highly viscous lithosphere move as realistic plate motion, which induces the plate-scale mantle flow (e.g., McNamara and Zhong, 2005; Zhang et al., 2010).

The former approach requires careful model setup to exactly reproduce the Earth's plate motion, and the trial-and-error method is used to achieve the desired results. Therefore, I applied the latter approach to the numerical model used in this study. For the details of the advantages and disadvantages of different mechanical surface boundary conditions, see Glišović and Forte (2015).

#### Basic Equations for Mantle Convection with Continental Drift

In the numerical model used in this study, the mantle was modeled as a Boussinesq fluid with an infinite Prandtl number and realistic Rayleigh number confined in three-dimensional (3-D) spherical-shell geometry ( $r, \theta, \phi$ ) with a thickness of 2867 km. Mantle convection was numerically solved by using a staggered-grid, finite-volume-based mantle convection code, ConvGS (e.g., Yoshida, 2008). The number of computational grids was taken to be  $128 (r) \times 128 (\theta) \times 384 (\phi) \times 2$  [for Yin and Yang grids (Yoshida and Kageyama, 2004, 2006)], and the numerical resolution was  $\sim 22$  km in vertical directions and  $\sim 78$  km in lateral directions at the surface. Impermeable, shear-stress-free conditions were imposed on both the top and bottom surface boundaries ( $r = r_1$  and  $r_0$ , respectively) of the spherical shell. However, in almost all the numerical models evaluated herein, the present-day plate motion was imposed for the first stage of the simulation as a velocity boundary condition, instead of

a shear-stress-free condition. The temperature conditions at the top and bottom surface boundaries were fixed at constant values, i.e.,  $T_0$  and  $T_1$ , respectively.

The dimensionless conservation equations for mass, momentum, and energy, which govern mantle convection under the Boussinesq approximation, and the advection equation for each material compositionally different from mantle materials, were expressed, respectively, as follows:

$$\nabla \cdot \mathbf{v} = 0, \quad (\text{S1})$$

$$-\nabla p + \nabla \cdot [\eta(\nabla \mathbf{v} + \nabla \mathbf{v}^T)] + \left( RaT - \sum_{i=1}^{N_{ph}} Rp_i \Gamma_i - \sum_{j=1}^{N_{ch}} Rc_j C_j \right) \xi^{-3} \mathbf{e}_r = 0, \quad (\text{S2})$$

$$\frac{\partial T}{\partial t} + \mathbf{v} \cdot \nabla T = \nabla^2 T + Q(t) \xi^{-2}, \quad (\text{S3})$$

$$\frac{\partial C_j}{\partial t} + \mathbf{v} \cdot \nabla C_j = 0, \quad (\text{S4})$$

where  $\mathbf{v}$  represents the velocity,  $p$  the dynamic pressure (positive for extension),  $\eta$  the viscosity,  $T$  the temperature,  $t$  the time,  $\Gamma_i$  the phase function ( $0 \leq \Gamma_i \leq 1$ ) (Christensen and Yuen, 1985),  $C_j$  the composition ( $0 \leq C_j \leq 1$ ),  $i$  the index of each phase in the mantle,  $j$  the index of each material compositionally different from mantle materials, and  $\mathbf{e}_r$  the radial component of the unit vector (positive for upward).

The dimensionless parameters were the thermal Rayleigh number  $Ra$ , the phase Rayleigh number  $Rp_i$ , the compositional Rayleigh number  $Rc_j$ , the time-dependent internal heating number  $Q$ , and the mantle/shell radius ratio  $\xi$ :

$$Ra \equiv \frac{\rho_0 \alpha_0 \Delta T g_0 b^3}{\eta_0 \kappa_0}, \quad Rp_i \equiv \frac{\Delta \rho_{ph(i)} g_0 b^3}{\eta_0 \kappa_0}, \quad Rc_j \equiv \frac{\Delta \rho_{ch(j)} g_0 b^3}{\eta_0 \kappa_0}, \quad (\text{S5})$$

$$Q(t) \equiv \frac{H(t) b^2}{\kappa_0 c_{p0} \Delta T}, \quad \xi \equiv \frac{b}{r_1}.$$

The definitions and values of the symbols used in the above equation are listed in Table S1.

The thermal Rayleigh number  $Ra$  was fixed at  $5.72 \times 10^7$ . The internal heat production depends on time and is influenced by the decay of radioactive elements in the chondritic mantle (Yoshida, 2014; Yoshida and Hamano, 2015) (Table S2). The olivine to wadsleyite phase transition at a reference depth of 410 km, the wadsleyite to ringwoodite phase transition at a depth of 520 km, and the ringwoodite to bridgmanite + magnesiowüstite phase decomposition at a depth of 660 km were imposed in the model (see Table S1).

The effective viscosity of the mantle material in the present model depends on its temperature, phase, and composition according to a dimensionless formulation:

$$\eta(T, \Gamma_i, C_1) = \eta_{ref}(\Gamma_i) \cdot \exp[\ln(\Delta \eta_C) C_1] \cdot \exp \left[ 2T_{ave}(t) \left( \frac{E}{T + T_{ave}(t)} - \frac{E}{2T_{ave}(t)} \right) \right], \quad (\text{S6})$$

where  $C_1$  is the composition that represents continental ( $C_1 = 1$ ) and mantle ( $C_1 = 0$ ) materials, and  $\Delta \eta_C$  is the viscosity ratio between the continental and mantle materials. The reference viscosity at each phase  $\eta_{ref}(\Gamma_{i=1,2})$  was set to 1 in the olivine, wadsleyite, and ringwoodite phases, and  $\Delta \eta_{lmn} \equiv \eta_{ref}(\Gamma_{i=3})$  was set to 30 (Bunge et al., 1996; Hager,

1991; Ricard et al., 1993) and 100 (Adam et al., 2014; Davies and Davies, 2009; Tosi et al., 2009; Yoshida, 2013) in the bridgmanite + magnesiowüstite phase.  $T_{ave}(t)$  is the dimensionless average temperature of the entire mantle at each time step, and  $E \equiv \ln(\Delta\eta_T)$  is the activation parameter that controls the effective viscosity contrast between the top surface and the underlying mantle; it was fixed at  $\Delta\eta_T = 10^3$  (Gordon, 2000; Tackley, 1993).

The time-dependent mantle heating rate is given by

$$H(t) = 0.9928C_0^U H^{U238} \exp\left(\frac{t \ln 2}{\tau_{1/2}^{U238}}\right) + 0.0071C_0^U H^{U235} \exp\left(\frac{t \ln 2}{\tau_{1/2}^{U235}}\right) + C_0^{Th} H^{Th} \exp\left(\frac{t \ln 2}{\tau_{1/2}^{Th}}\right) + 1.19 \times 10^{-4} C_0^K H^{K40} \exp\left(\frac{t \ln 2}{\tau_{1/2}^{K40}}\right), \quad (S7)$$

where  $C_0^U$ ,  $C_0^{Th}$ ,  $C_0^K$  are the concentrations of each radioactive isotope (uranium, thorium, and potassium),  $H^{U238}$ ,  $H^{U235}$ ,  $H^{Th}$ ,  $H^{K40}$  are the rates of heat release of each isotope, and  $\tau_{1/2}^{U238}$ ,  $\tau_{1/2}^{U235}$ ,  $\tau_{1/2}^{Th}$ ,  $\tau_{1/2}^{K40}$  are the half-lives of each isotope (Turcotte and Schubert, 2014). The values are based on chondritic meteorites (Turcotte and Schubert, 2014) (Table S2), although the mantle is strongly depleted in K and the choice may not be the best reference. However, the resulting radioactive heat production rate per unit mass at the present is estimated as  $3.50 \times 10^{-12} \text{ W kg}^{-1}$  (Table S1), and considering the mass of the mantle is  $4.0 \times 10^{24} \text{ kg}$  (Turcotte and Schubert, 2014), total heat production of the whole mantle is estimated as  $\sim 14 \text{ TW}$ . This value is comparable to that derived from the evidence obtained in geodynamics, seismology, and mineral physics investigations,  $\sim 12\text{--}14 \text{ TW}$  (Lay et al., 2008). Actually, in the present numerical model, the calculated basal heating ratio (i.e., the ratio of total surface integration of heat flow at the core–mantle boundary to that at the top surface,  $\gamma_b$ ) at 0 m.y. is  $\sim 49\%$  (Fig. DR7) and the calculated  $\gamma_b$  for 250 m.y. for each model ranges between  $\sim 40\%$  to  $\sim 75\%$ , which is consistent with that from the discussion on the thermal heat budget whereby significant heat comes from the core and the deep mantle layer above the core–mantle boundary (Davies, 2009); previous independent numerical models of thermally steady-state mantle convection produce values ranging from 39% to 71% (Zhong et al., 2007) and 35% to 70% (Zhang et al., 2010).

The present-day plate motion compiled from NNR-MORVEL56 (Argus et al., 2011), which is a current plate motion model in the no-net-rotation (NNR) reference frame for 56 plates based on a widely published digital plate boundaries model (Bird, 2003), was imposed for the first stage of the simulation as a velocity boundary condition at the top surface boundary (Fig. DR1C) instead of a shear-stress-free condition. Because the NNR model is based on the motion of each plate with respect to the weight average of all of the global plate velocities, it is useful for the modeling of mantle flow while removing rigid rotation (i.e., toroidal component of degree 1 is zero).

### Initial Settings for the Simulations

On the basis of the thermal boundary layer theory (Turcotte and Schubert, 2014), the initial condition for the radial (depth) profile of dimensionless temperature with a thermal boundary layer(s) at the top and bottom surface boundaries can be given by the following non-dimensionless form:

$$T(r) = (T_{im} - T_{top}) \cdot \operatorname{erf}\left(\frac{r_1 - r}{2\sqrt{\tau_p}}\right) + \omega \cdot (T_{bot} - T_{im}) \cdot \left[1 - \operatorname{erf}\left(\frac{r - r_0}{2\sqrt{\tau_p}}\right)\right], \quad (\text{S8})$$

where  $\tau_p = (\kappa_0 / r_1^2) \bar{\tau}_p$ ; here,  $\bar{\tau}_p$  is the heat conduction time corresponding to the thickness of thermal boundary layers of 100 km. Eq. S8 means that there is no thermal boundary layer at the bottom surface for the initial temperature field when  $\omega$  is set to 0.0. The initial mantle temperature  $T_{im}$  can be approximated by a simple heat balance equation for the mantle (Schubert et al., 2001):

$$4\pi r_1^2 k_0 \frac{T_{im} - T_0}{\delta_1} = 4\pi r_0^2 k_0 \frac{T_1 - T_{im}}{\delta_0} + \frac{4}{3} H_0 \pi (r_1^3 - r_0^3), \quad (\text{S9})$$

where the definitions of the symbols are as listed in Table S1. Therefore, the initial mantle temperature  $T_{im}$  is:

$$T_{im} = T_0 + \frac{\delta_0 \delta_1}{k_0 (\delta_0 r_1^2 + \delta_1 r_0^2)} \left( \frac{r_0^2 k_0 T_1}{\delta_0} + \frac{r_1^2 k_0 T_0}{\delta_1} + \frac{H_0}{3} (r_1^3 - r_0^3) \rho_0 \right). \quad (\text{S10})$$

Substituting the thickness of the thermal boundary layers at the top and bottom surfaces,  $\delta_1 = \delta_0 = 100$  km, and the physical values in Table S1 into Eq. S10, the non-dimensional  $T_{im}$  was estimated to be  $\sim 0.38$ .

In the present model, the seismic velocity anomaly was assumed to depend on the temperature perturbation alone. The initial state of the lateral temperature anomaly in the mantle at present was derived from the whole-mantle P-wave tomographic model, GAP\_P4 (Obayashi et al., 2013) (Fig. DR1A). The seismic velocity anomaly  $\delta V_P$  from GAP\_P4 was converted to the temperature anomaly  $\delta T_P$  as follows:

$$\delta T(r, \theta, \phi) = -\frac{1}{A_{V_P T}(r)} \delta V_P(r, \theta, \phi), \quad (\text{S11})$$

where  $\delta V_P$  is the deviation from a preliminary reference Earth model, PREM (Dziewonski and Anderson, 1981). The temperature derivative of the seismic velocity anomaly as a function of radius (depth) was defined based on some mineral physics experiments (Karato, 2008; Yoshida, 2012b) (Fig. DR1B):

$$A_{V_P T}(r) \equiv -\frac{\partial \delta V_P}{\partial T}. \quad (\text{S12})$$

The low seismic-velocity-anomaly in the shallower part of the upper mantle from the seismic tomographic model does not always indicate the positive temperature anomaly because of various sorts of chemical effects. Therefore, following the previous model (Conrad and Lithgow-Bertelloni, 2006), the temperature anomaly was set to be zero in the low seismic-velocity-anomaly region above a depth of 300 km as a reference initial temperature field (Case T-1). For Case T-1 shown in Fig. DR1A, the dimensionless initial temperature field in the mantle at the beginning of the simulations was

$$T(r, \theta, \phi) = T(r) + \delta T(r, \theta, \phi). \quad (\text{S13})$$

The distribution of the present-day continents was compiled from ETOPO1, a 1 arc-minute global topographic model of the Earth's surface (Amante and Eakins, 2009). The thickness of the continents was initially set to  $\sim 200$  km. The density difference between the chemically buoyant continents and the ambient mantle was taken to be  $-100 \text{ kg m}^{-3}$  (Poudjom Djomani et al., 2001; Rolf and Tackley, 2011). The viscosity ratio between the highly viscous continents and the ambient mantle ( $\Delta \eta_c$ ) was taken to

be  $10^3$  (Doin et al., 1997; Lenardic and Moresi, 1999; Yoshida, 2012a; Yoshida and Hamano, 2015).

## ANALYSES OF THE NUMERICAL RESULTS

The temperature anomaly of the mantle interior at each radius for each time-step was estimated as follows:

$$\delta T(r) = T(r, \theta, \phi) - \langle T(r) \rangle, \quad (\text{S14})$$

where  $\langle T(r) \rangle$  is the laterally averaged temperature at each radius.

The root-mean square (RMS) velocities at the top surface ( $V_{sur}$ ) and the mantle interior ( $V_{vol}$ ) at each elapsed time were estimated as follows:

$$V_{sur}(t) = \sqrt{\frac{\int_{\theta=0}^{\pi} \int_{\phi=0}^{2\pi} (|v_{s\theta}|^2 + |v_{s\phi}|^2) r_1^2 \sin \theta d\theta d\phi}{\int_{\theta=0}^{\pi} \int_{\phi=0}^{2\pi} r_1^2 \sin \theta d\theta d\phi}}, \quad (\text{S15})$$

$$V_{vol}(t) = \sqrt{\frac{\int_{r=r_i}^{r_o} \int_{\theta=0}^{\pi} \int_{\phi=0}^{2\pi} (|v_r|^2 + |v_{\theta}|^2 + |v_{\phi}|^2) r^2 \sin \theta dr d\theta d\phi}{\int_{r=r_i}^{r_o} \int_{\theta=0}^{\pi} \int_{\phi=0}^{2\pi} r^2 \sin \theta dr d\theta d\phi}},$$

where  $r_o$  and  $r_i$  are the radii at the outer and inner boundary, respectively, and  $v_{s\theta}$  and  $v_{s\phi}$  are the latitudinal and longitudinal velocities at the surface boundary at  $r = r_1$ , respectively. In Figs. 2 and DR4, the RMS velocities of the mantle interior were separately calculated in the upper mantle at depths of 100 to 660 km and the lower mantle at depths of 660 to 2867 km. In addition, they were calculated for the cold mantle region with a negative temperature anomaly ( $\delta T \leq 0$ ) and for the hot mantle with a positive temperature anomaly ( $\delta T \geq 0$ ).

## On Toroidal Energy of Mantle Flow

The kinematic energy of the convective fluid under the gravity field is mathematically divided into poloidal and toroidal energies. Previous numerical studies suggest that the toroidal energy is about 10% of the poloidal energy in the mantle convection with temperature-dependent viscosity (Hsui et al., 1995), and the ratio of toroidal energy becomes larger if a combination of tectonic plates and plate boundaries with strongly lateral variable viscosity are considered in mantle convection (Yoshida et al., 2001). The results of the present study suggest that the toroidal energy originating only from the temperature-dependent viscosity is not sufficient to drive the Earth-like continental drift and that the strongly lateral variable viscosity originating from the plate tectonics is needed to realize continental drift.

## SUPPLEMENTARY FIGURES AND TABLES

I prepared seven supplementary figures (Figs. DR1 to DR7) and three supplementary tables (Tables DR1 to DR3) for this study.

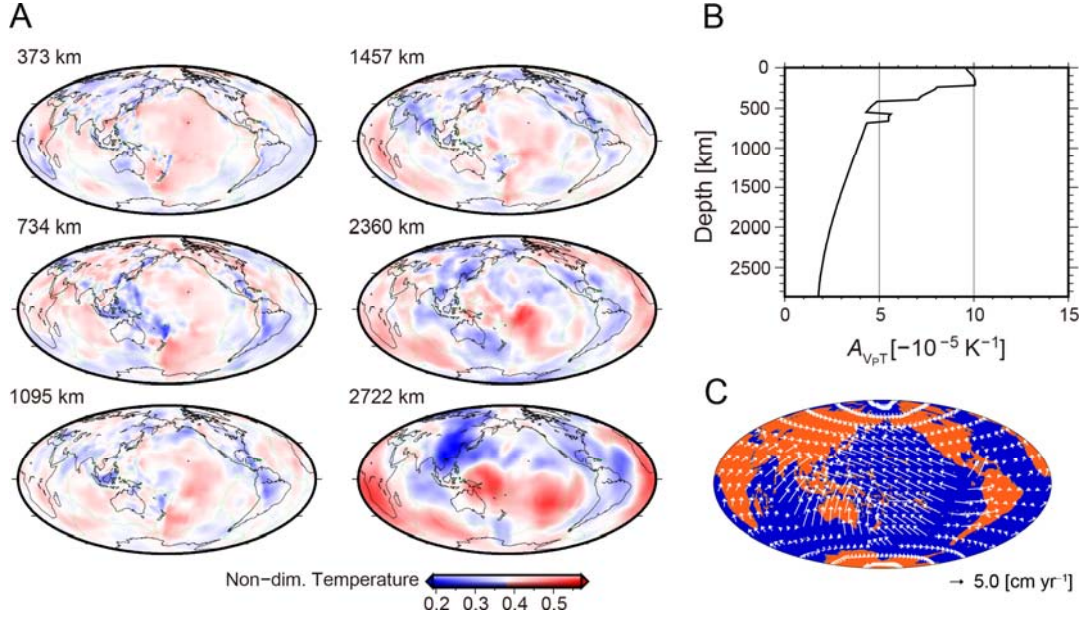


**Figure DR1.** (A) Initial temperature field of the mantle at depths of 373 km, 734 km, 1095 km, 1457 km, 2360 km, and 2722 km for Case T-1. Blue and red areas indicate negative and positive temperature anomalies from the average mantle temperature at each depth. The non-dimensional temperature of 0.1 corresponds to 250 K. (B) The depth profile of the temperature derivatives of P-wave velocity anomalies  $A_{V_{PT}}$  in Eq. S10 based on mineral physics experiments (Karato, 2008). (C) Global map for the imposed plate motion from NNR-MORVEL56 (Argus et al., 2011) at the beginning of the simulations.

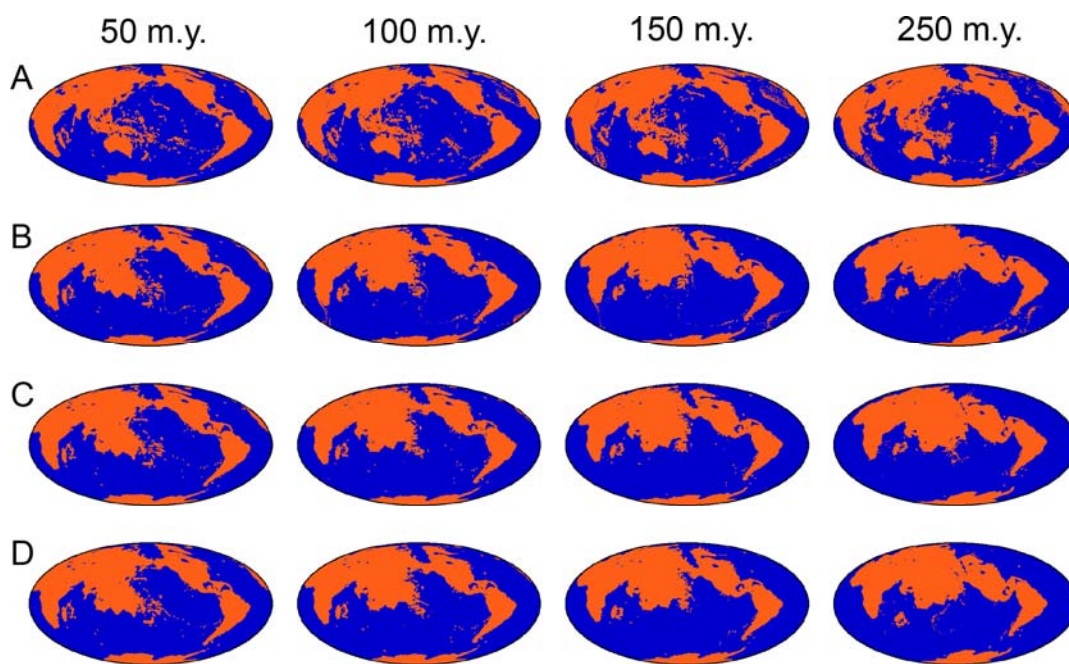
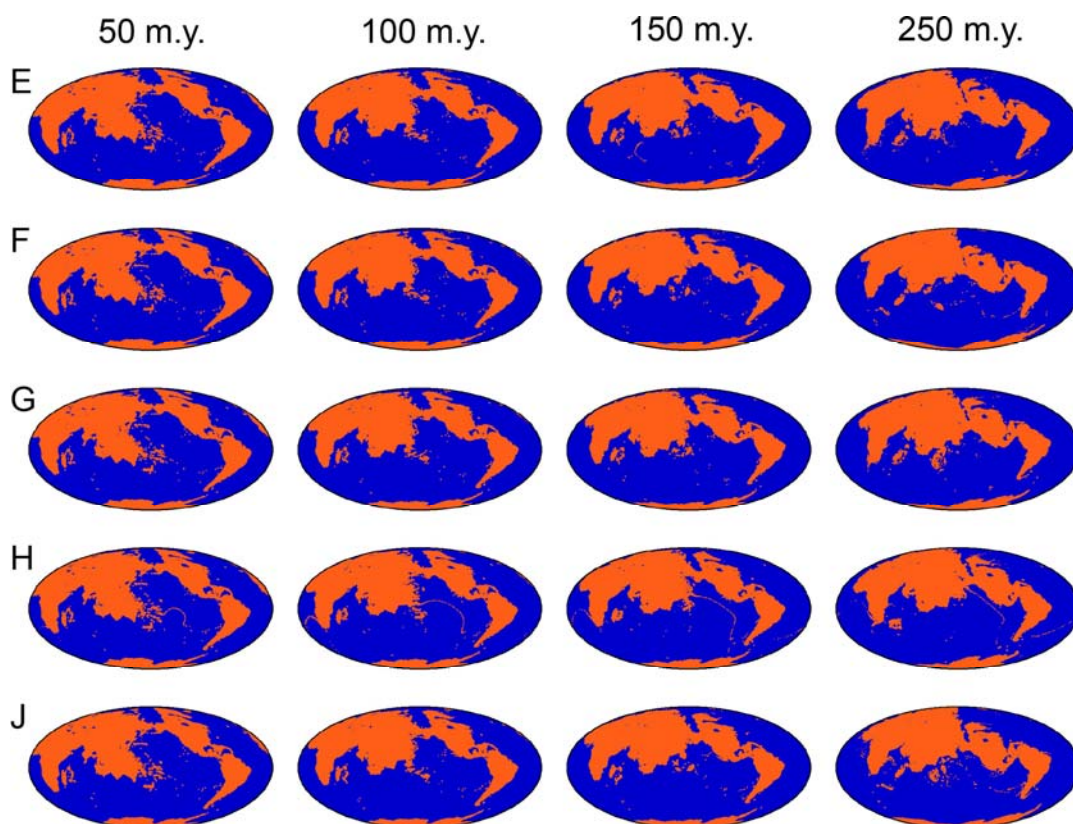
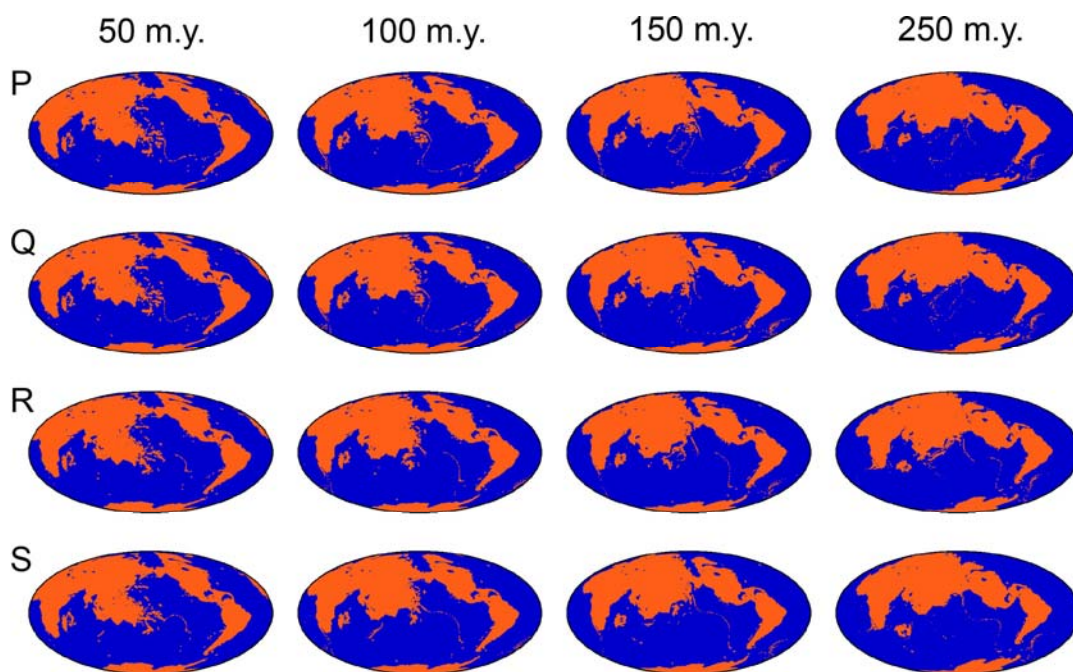


**Figure DR2.** Numerical results of continental drift (orange) after 50, 100, 150, and 250 million years (m.y.) from the present for Models (A) I-0, (B) I, (C) II, and (D) III.



*Cont.* Numerical results of continental drift (orange) after 50, 100, 150, and 250 million years (m.y.) from the present for Models (E) IV, (F) V, (G) VI, (H) VII, and (J) VIII.





*Cont.* Numerical results of continental drift (orange) after 50, 100, 150, and 250 million years (m.y.) from the present for Models (P) I-0.1, (Q) I-0.5, (R) I-5, and (S) I-10.

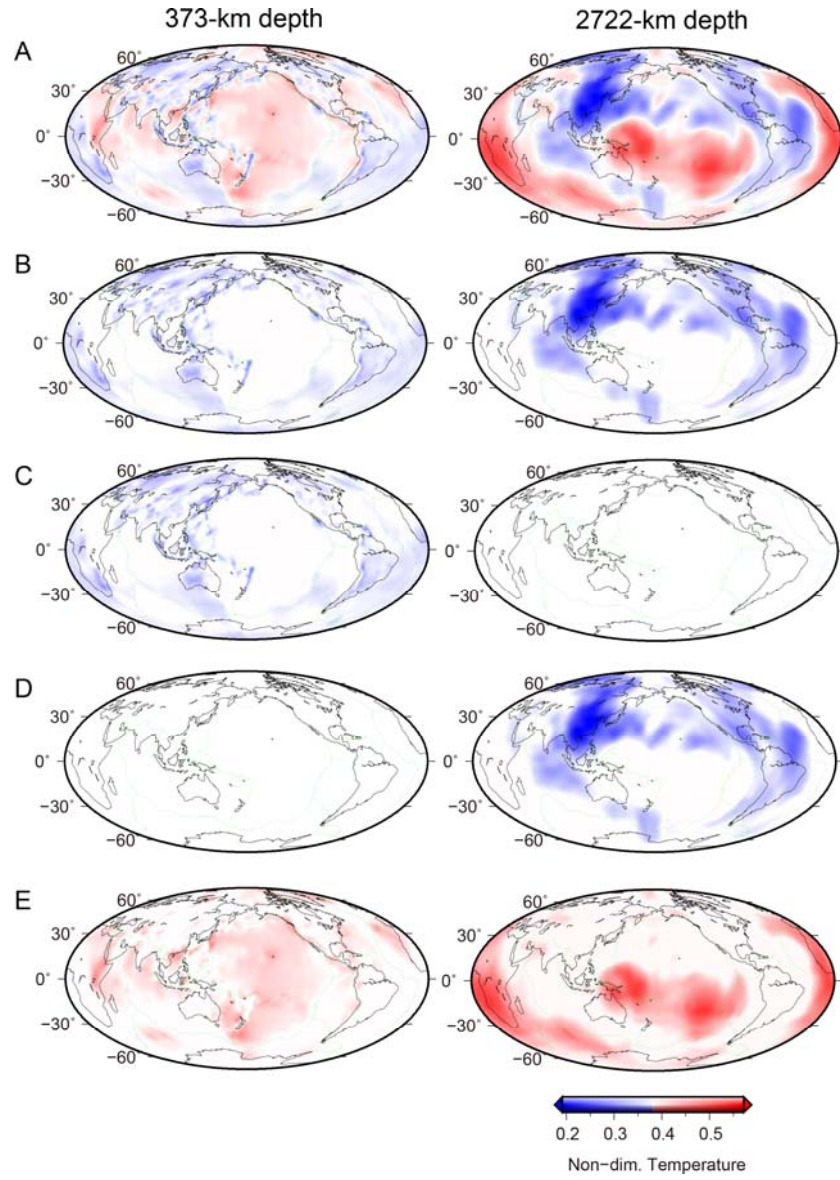


**Figure DR3.** Initial temperature field of the mantle at depths of 373 km and 2722 km for Cases (A) T-1, (B) T-2, (C) T-3, (D) T-4, and (E) T-5. Blue and red areas indicate negative and positive temperature anomalies from the average mantle temperature at each depth. The non-dimensional temperature of 0.1 corresponds to 250 K.

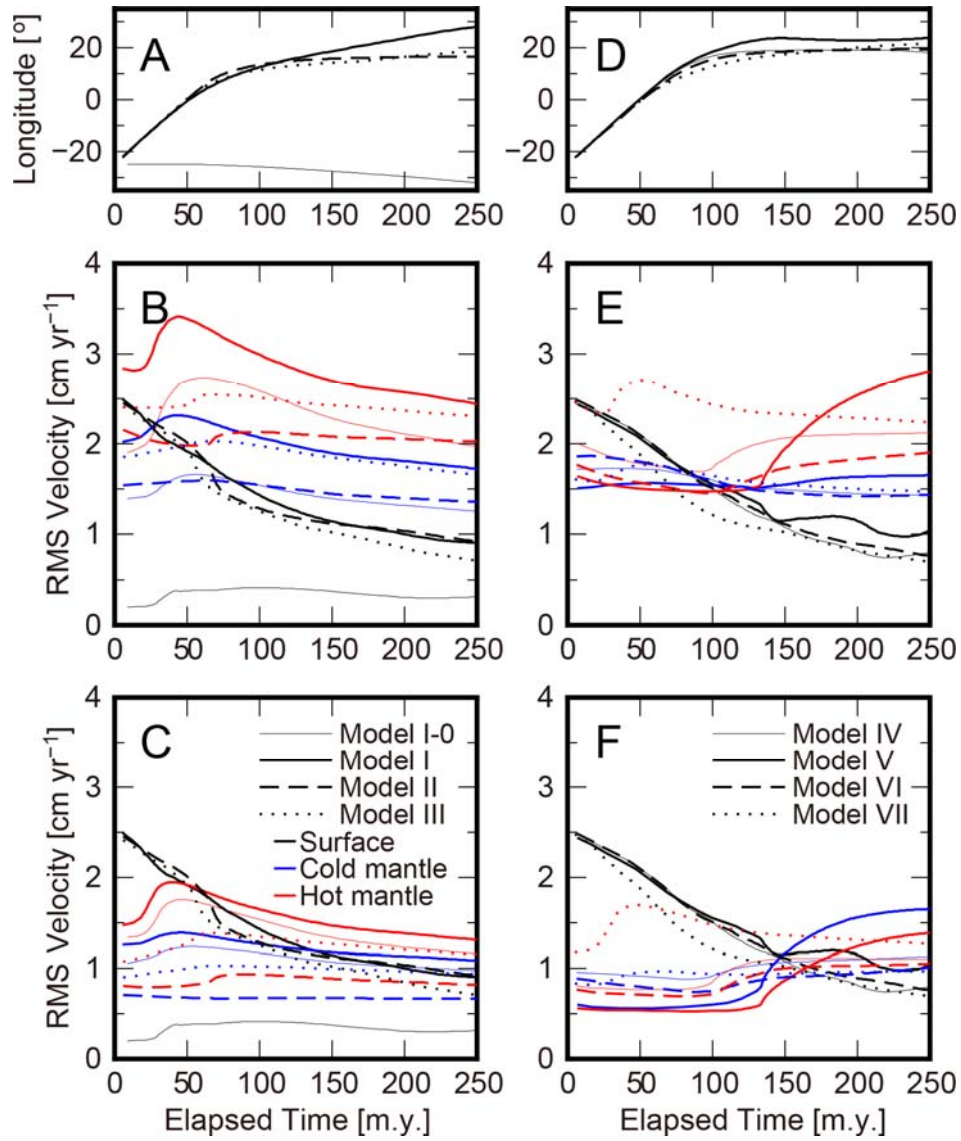


**Figure DR4.** Same as Fig. 2 in the main text for (A, B, C) Models I-0, I, II, and III and (D, E, F) Models IV, V, VI, and VII.

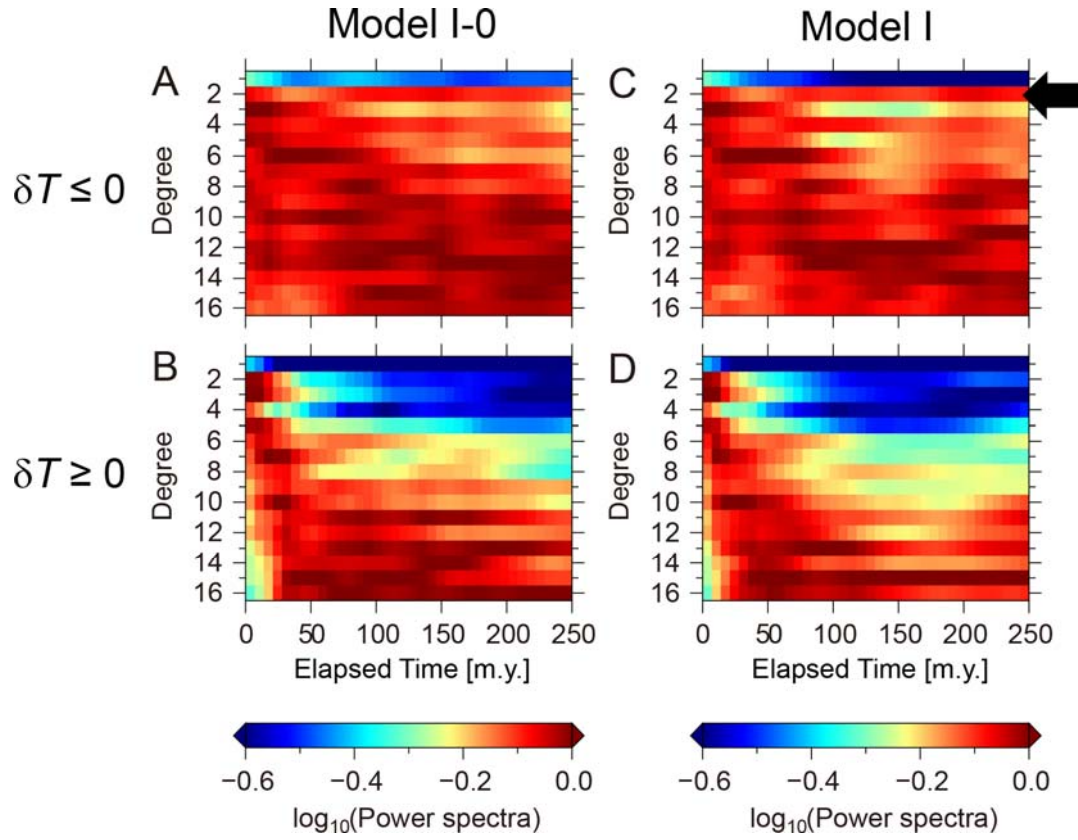


**Figure DR5.** Heterogeneity spectrogram of the temperature field in the lower mantle under depths of 660 km for (A–B) Model I-0 and (C–D) Model I. The power spectrum was analyzed separately for the (A–C) negative temperature anomalies (i.e.,  $\delta T \leq 0$ ) and (B–D) positive temperature anomalies (i.e.,  $\delta T \geq 0$ ) at each depth (see Supplementary materials). The red to blue color range shows strong to weak thermal heterogeneity at spherical harmonic degrees of 1 to 16. The power spectra were normalized by the maximum values at each elapsed time.

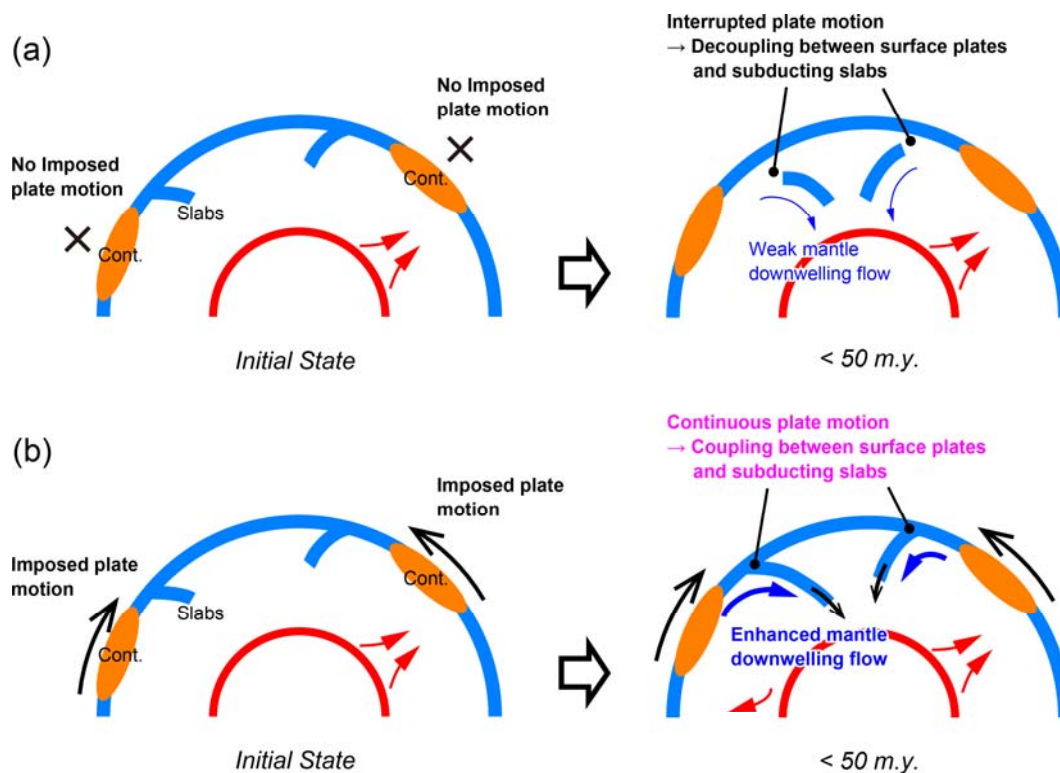


**Figure DR6.** Illustrations showing the effect of imposed plate motions on the subsequent continental drift and mantle flow. In the model without imposed plate motions for the first stage of simulation (a), surface plates do not couple with the subducting slabs and the weak mantle downwelling flow can hardly move the continental plates. On the other hand, in the model with imposed plate motions for the first stage of simulation (b), the surface plates couple with the subducting slabs, which brings about the plate-scale flow and enhances underlying mantle downwelling flow; this is referred to as "plate motion-driving flow" (see text for details).



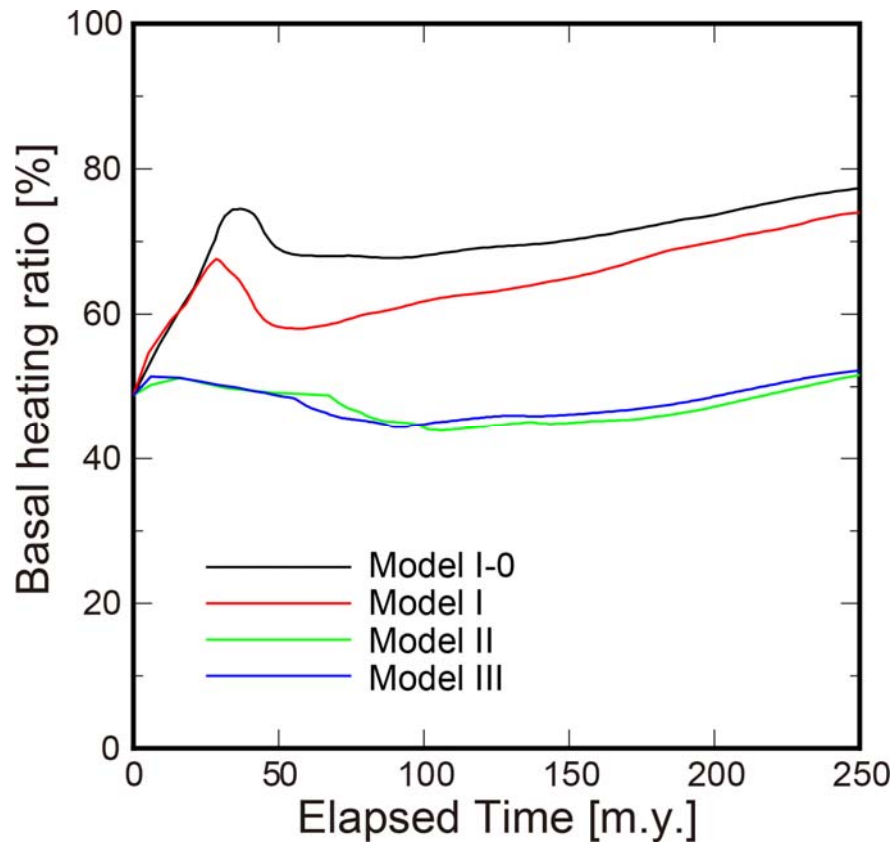


**Figure DR7.** Temporal variations for the basal heating ratio (i.e., the ratio of total surface integration of heat flow at the core–mantle boundary to that at the top surface). Black, red, green, and blue lines are for Models I-0, I, II, and III, respectively.

**Table DR1.** Model parameters used in the present study.

Symbol	Definition	Value	Unit	Refs.
$g_0$	Reference gravitational acceleration	9.81	$\text{m s}^{-2}$	a
$\rho_0$	Reference density of mantle	3300	$\text{kg m}^{-3}$	a
$\alpha_0$	Reference thermal expansivity of mantle	$3 \times 10^{-5}$	$\text{K}^{-1}$	a
$T_0$	Temperatures at the Earth's surface	273	K	a
$T_1$	Temperatures at the core–mantle boundary	2773	K	a
$\Delta T$	Temperature difference across the mantle	2500	K	a
$r_1$	Radius of the Earth's surface	6371	km	a
$r_0$	Radius of the core–mantle boundary	3504	km	a
$b$	Thickness of mantle	2867	km	a
$\kappa_0$	Reference thermal diffusivity of mantle	$10^{-6}$	$\text{m}^2 \text{s}^{-1}$	a
$k_0$	Reference thermal conductivity	4.125	$\text{W m}^{-1} \text{K}^{-1}$	a
$\eta_0$	Reference viscosity of upper mantle	$10^{21}$	Pa s	a
$c_{p0}$	Reference specific heat at constant pressure of mantle	1250	$\text{J kg}^{-1} \text{K}^{-1}$	a
$H$	Radioactive heat production rate per unit mass	$t$ -dep.	$\text{W kg}^{-1}$	a
$H_0$	Radioactive heat production rate per unit mass at the present	$3.50 \times 10^{-12}$	$\text{W kg}^{-1}$	a
–	Clapeyron slope at 410-, 520-, and 660-km phase transitions	1.6, 4.3, –2.5	$\text{MPa K}^{-1}$	b
$\Delta \rho_{ph(i)}$	Density contrast at 410-, 520-, and 660-km phase transitions	7%, 3% 10%	–	b
$\Delta \eta_c$	Viscosity contrast between continents ( $C_1 = 1$ ) and oceans ( $C_1 = 0$ )	$10^3$	–	c–f
$\Delta \rho_{ch(j)}$	Density contrast between continents and surrounding mantle	100	$\text{kg m}^{-3}$	g, h

*Dimensionless parameters*

Symbol	Definition	Value	Equation
$Ra$	Thermal Rayleigh number	$5.72 \times 10^7$	S5
$Rp_i$	Phase Rayleigh numbers for 410-km ( $i = 1$ ), 520-km ( $i = 2$ ), and 660-km ( $i = 3$ ) phase transitions	$5.34 \times 10^7$ , $2.29 \times 10^7$ , $7.63 \times 10^7$	S5
$Rc_j$	Compositional Rayleigh number for continents ( $j = 1$ )	$-2.31 \times 10^7$	S5
$Q$	Internal heating number	$t$ -dep.	S5
$Q_0$	Internal heating number at the present	9.19	S5
$\xi$	Mantle/shell radius ratio	0.45	S5

Value:  $t$ -dep., time-dependent. References (Refs.): a (Turcotte and Schubert, 2014); b (Schubert et al., 2001); c (Yoshida and Hamano, 2015); d (Yoshida, 2012a); e (Lenardic and Moresi, 1999); f (Doin et al., 1997); g (Poudjom Djomani et al., 2001); h (Rolf et al., 2012).

**Table DR2.** Rates of heat release  $H$ , half-lives  $\tau_{1/2}$ , and concentrations  $C_0$  of the radioactive isotopes in chondritic meteorites (Turcotte and Schubert, 2014).

Isotope	$H [\text{W kg}^{-1}]$	$\tau_{1/2} [\text{yr}]$	$C_0 [\text{kg kg}^{-1}]$
$^{238}\text{U}$	$9.46 \times 10^{-5}$	$4.47 \times 10^9$	–
$^{235}\text{U}$	$5.69 \times 10^{-4}$	$7.04 \times 10^8$	–
$\text{U}$	$9.81 \times 10^{-5}$	–	$8 \times 10^{-9}$
$^{232}\text{Th}$	$2.64 \times 10^{-5}$	$1.40 \times 10^{10}$	$29 \times 10^{-9}$
$^{40}\text{K}$	$2.92 \times 10^{-5}$	$1.25 \times 10^9$	–
$\text{K}$	$3.48 \times 10^{-9}$	–	$56 \times 10^{-5}$

**Table DR3.** Models examined in the present study.

Model	$\Delta\eta_{lmn}$	Initial T Case	Negative $\delta T$ (cold) mantle	positive $\delta T$ (hot) mantle	$\omega$	$\Delta t_p$	$d_{vj}$	Figs.
<i>Variation in the viscosity structure</i>								
I	30	T-1	whole depth	$\geq 300$ -km dep.	1.0	1	660	1, 2, DR2B, DR4, DR5, DR7
II	100	T-1	whole depth	$\geq 300$ -km dep.	1.0	1	660	DR2C, DR4, DR5, DR7
III	100	T-1	whole depth	$\geq 300$ -km dep.	1.0	1	1000	DR2D, DR4, DR5, DR7
<i>Variation in the initial pattern of mantle temperature</i>								
IV	30	T-2	whole depth	no	0.0	1	660	DR2E, DR4
V	30	T-3	$\leq 660$ -km dep.	no	0.0	1	660	DR2F, DR4
VI	30	T-4	$\geq 660$ -km dep.	no	0.0	1	660	DR2G, DR4
VII	30	T-5	no	$\geq 300$ -km dep.	1.0	1	660	DR2H, DR4
VIII	30	T-6	no	no	0.0	1	660	DR2J
<i>Variation in the time interval of the imposed plate motion</i>								
I-0	30	T-1	whole depth	$\geq 300$ -km dep.	1.0	0	660	1, 2, DR2A, DR4, DR5, DR7
I-5	30	T-1	whole depth	$\geq 300$ -km dep.	1.0	5	660	2, DR2P
I-10	30	T-1	whole depth	$\geq 300$ -km dep.	1.0	10	660	2, DR2Q
I-0.5	30	T-1	whole depth	$\geq 300$ -km dep.	1.0	0.5	660	2, DR2R
I-0.1	30	T-1	whole depth	$\geq 300$ -km dep.	1.0	0.1	660	2, DR2S

Unit:  $\Delta t_p$ , [m.y.];  $d_{vj}$ , [km]



## REFERENCES CITED

- Adam, C., Yoshida, M., Suetsugu, D., Fukao, Y., and Cadio, C., 2014, Geodynamic modeling of the South Pacific superswell: *Phys. Earth Planet. Int.*, v. 229, p. 24-39.
- Amante, C., and Eakins, B. W., 2009, ETOPO1 1 Arc-Minute Global Relief Model: Procedures, Data Sources and Analysis. NOAA Technical Memorandum NESDIS NGDC-24, 19 pp, March 2009.
- Argus, D. F., Gordon, R. G., and Demets, C., 2011, Geologically current motion of 56 plates relative to the no-net-rotation reference frame: *Geochem. Geophys. Geosyst.*, v. 12, no. 11, p. Q11001.
- Bird, P., 2003, An updated digital model of plate boundaries: *Geochem. Geophys. Geosyst.*, v. 4, no. 3, p. 1027.
- Bunge, H.-P., Richards, M. A., and Baumgardner, J. R., 1996, The effect of depth dependent viscosity on the planform of mantle convection: *Nature*, v. 379, p. 436-438.
- Christensen, U. R., and Yuen, D. A., 1985, Layered convection induced by phase transitions: *J. Geophys. Res.*, v. 90, no. B12, p. 10291-10300.
- Conrad, C. P., and Lithgow-Bertelloni, C., 2006, Influence of continental roots and asthenosphere on plate-mantle coupling: *Geophys. Res. Lett.*, v. 33, no. 5, p. L05312.
- Davies, D. R., and Davies, J. H., 2009, Thermally-driven mantle plumes reconcile multiple hot-spot observations: *Earth Planet Sci. Lett.*, v. 278, no. 1-2, p. 50-54.
- Davies, G. F., 2009, Reconciling the geophysical and geochemical mantles: Plume flows, heterogeneities, and disequilibrium: *Geochem. Geophys. Geosyst.*, v. 10, no. 10, p. Q10008.
- Doin, M.-P., Fleitout, L., and Christensen, U., 1997, Mantle convection and stability of depleted and undepleted continental lithosphere: *J. Geophys. Res.*, v. 102, no. B2, p. 2771-2787.
- Dziewonski, A. M., and Anderson, D. L., 1981, Preliminary reference earth model: *Phys. Earth Planet. Int.*, v. 25, p. 297-356.
- Glišović, P., and Forte, A. M., 2015, Importance of initial buoyancy field on evolution of mantle thermal structure: Implications of surface boundary conditions *Geosci. Front.*, v. 6, no. 1, p. 3-22.
- Gordon, R. G., 2000, Diffuse oceanic plate boundaries: Strain rates, vertically averaged rheology, and comparisons with narrow plate boundaries and stable plate

- interiors, *in* Richards, M. A., Gordon, R., and van der Hilst, R. D., eds., The history and dynamics of global plate motions, Geophys. Monograph Series, Volume 121: Washington D.C., Am. Geophys. Union, p. 143-159.
- Hager, B. H., 1991, Mantle viscosity: A comparison of models from postglacial rebound and from the geoid, plate driving forces, and advected heat flux, *in* R. Sabatini, Lambeck, K., and E. Boschi, eds., Glacial Isostasy, Sea-Level and Mantle Rheology: Kluwer Academic Publishers, Dordrecht, The Netherlands, Kluwer Academic Publishers, Dordrecht, The Netherlands, p. 493-513.
- Hsui, A. T., Yang, W.-S., and Baumgardner, J. R., 1995, A preliminary study of the effects of some flow parameters in the generation of poloidal and toroidal energies within a 3-D spherical thermal-convective system with variable viscosity: *Pure Appl. Geophys.*, v. 145, no. 3, p. 487-503.
- Karato, S., 2008, Deformation of Earth materials: Introduction to the rheology of the solid Earth, U. K. , Cambridge Univ. Press.
- Lay, T., Hernlund, J., and Buffett, B. A., 2008, Core-mantle heat flow: *Nat. Geosci.*, v. 1, p. 25-32.
- Lenardic, A., and Moresi, L.-N., 1999, Some thoughts on the stability of cratonic lithosphere: effects of buoyancy and viscosity: *J. Geophys. Res.*, v. 104, no. B6, p. 12747-12758.
- McNamara, A. K., and Zhong, S., 2005, Thermochemical structures beneath Africa and the Pacific ocean: *Nature*, v. 437, p. 1136-1139.
- Obayashi, M., Yoshimitsu, J., Nolet, G., Fukao, Y., Shiobara, H., Sugioka, H., Miyamachi, H., and Gao, Y., 2013, Finite frequency whole mantle P wave tomography: Improvement of subducted slab images: *Geophys. Res. Lett.*, v. 40, no. 21, p. 5652-5657.
- Poudjom Djomani, Y. H., O'Reilly, S. Y., Griffin, W. L., and Morgan, P., 2001, The density structure of subcontinental lithosphere through time: *Earth Planet Sci. Lett.*, v. 184, no. 3-4, p. 605-621.
- Ricard, Y., Richards, M., Lithgow-Bertelloni, C., and Stunff, Y. L., 1993, A geodynamic model of mantle density heterogeneity: *J. Geophys. Res.*, v. 98, no. B12, p. 21895-21909.
- Rolf, T., Coltice, N., and Tackley, P. J., 2012, Linking continental drift, plate tectonics and the thermal state of the Earth's mantle: *Earth Planet Sci. Lett.*, v. 351-352, p. 134-146.
- Rolf, T., and Tackley, P. J., 2011, Focussing of stress by continents in 3D spherical mantle convection with self-consistent plate tectonics: *Geophys. Res. Lett.*, v. 38,

p. L18301.

- Schubert, G., Turcotte, D. L., and Olson, P., 2001, *Mantle Convection in the Earth and Planets*, UK, Cambridge Univ. Press, 956 p.:
- Stadler, G., Gurnis, M., Burstedde, C., Wilcox, L. C., Alisic, L., and Ghattas, O., 2010, The dynamics of plate tectonics and mantle flow: From local to global scales: *Science*, v. 329, no. 5995, p. 1033-1038.
- Tackley, P., 1993, Effects of strongly temperature-dependent viscosity on time-dependent, three-dimensional models of mantle convection: *Geophys. Res. Lett.*, v. 20, no. 20, p. 2187-2190.
- Tosi, N., Čadež, O., and Martinec, Z., 2009, Subducted slabs and lateral viscosity variations: effects on the long-wavelength geoid: *Geophys. J. Int.*, v. 179, no. 2, p. 813-826.
- Turcotte, D. L., and Schubert, G., 2014, *Geodynamics*, UK, Cambridge Univ. Press, 636 p.:
- Yoshida, M., 2008, Mantle convection with longest-wavelength thermal heterogeneity in a 3-D spherical model: Degree one or two?: *Geophys. Res. Lett.*, v. 35, p. L23302.
- , 2012a, Dynamic role of the rheological contrast between cratonic and oceanic lithospheres in the longevity of cratonic lithosphere: A three-dimensional numerical study: *Tectonophysics*, v. 532-535, p. 156-166.
- , 2012b, Plume's buoyancy and heat fluxes from the deep mantle estimated by an instantaneous mantle flow simulation based on the S40RTS global seismic tomography model: *Phys. Earth Planet. Int.*, v. 210-211, p. 63-74.
- , 2013, The role of harzburgite layers in the morphology of subducting plates and the behavior of oceanic crustal layers: *Geophys. Res. Lett.*, v. 40, no. 20, p. 5387-5392.
- , 2014, Effects of various lithospheric yield stresses and different mantle-heating modes on the breakup of the Pangea supercontinent: *Geophys. Res. Lett.*, v. 41, no. 9, p. 3060-3067.
- Yoshida, M., and Hamano, Y., 2015, Pangea breakup and northward drift of the Indian subcontinent reproduced by a numerical model of mantle convection: *Sci. Rep.*, v. 5, p. 8407.
- Yoshida, M., Honda, S., Kido, M., and Iwase, Y., 2001, Numerical simulation for the prediction of the plate motions: Effects of lateral viscosity variations in the lithosphere: *Earth Planets Space*, v. 53, no. 7, p. 709-721.
- Yoshida, M., and Kageyama, A., 2004, Application of the Yin-Yang grid to a thermal

- convection of a Boussinesq fluid with infinite Prandtl number in a three-dimensional spherical shell: *Geophys. Res. Lett.*, v. 31 no. 12, p. L12609.
- , 2006, Low-degree mantle convection with strongly temperature- and depth-dependent viscosity in a three-dimensional spherical shell: *J. Geophys. Res.*, v. 111, no. B3, p. B03412.
- Yoshida, M., and Nakakuki, T., 2009, Effects on the long-wavelength geoid anomaly of lateral viscosity variations caused by stiff subducting slabs, weak plate margins and lower mantle rheology: *Phys. Earth Planet. Int.*, v. 172, no. 3-4, p. 278-288.
- Zhang, N., Zhong, S., Leng, W., and Li, Z.-X., 2010, A model for the evolution of the Earth's mantle structure since the Early Paleozoic: *J. Geophys. Res.*, v. 115, p. B06401.
- Zhong, S., and Davies, G. F., 1999, Effects of plate and slab viscosities on the geoid: *Earth Planet. Sci. Lett.*, v. 170, p. 487-496.
- Zhong, S., Zhang, N., Li, Z.-X., and Roberts, J. H., 2007, Supercontinent cycles, true polar wander, and very long-wavelength mantle convection: *Earth Planet. Sci. Lett.*, v. 261, no. 3-4, p. 551-564.